Coexistence of near-E_F Flat Band and Van Hove Singularity in a Two-Phase Superconductor

Xuezhi Chen,[1,2,3,*] Le Wang,[4,5,*] Jun Ishizuka,[6,*] Renjie Zhang,[2,3,7,*] Kosuke Nogaki,[8] Yiwei Cheng,[1,2,3] Fazhi Yang,[2] Zhenhua Chen,[9] Fangyuan Zhu,[9] Zhengtai Liu,[9] Jiawei Mei,[4,5] Youichi Yanase,[8,†] Baiqing Lv,[2,10,11,‡] and Yaobo Huang[9,§]

[1]*Shanghai Institute of Applied Physics, Chinese Academy of Sciences, Shanghai 201800, China*
[2]*Tsung-Dao Lee Institute, Shanghai Jiao Tong University, Shanghai 200240, China*
[3]*University of Chinese Academy of Sciences, Beijing 100049, China*
[4]*Shenzhen Institute for Quantum Science and Engineering,*
Southern University of Science and Technology, Shenzhen 518055, China
[5]*International Quantum Academy, Shenzhen 518048, China*
[6]*Faculty of Engineering, Niigata University, Ikarashi, Niigata 950-2181, Japan*
[7]*Beijing National Laboratory for Condensed Matter Physics and Institute of Physics,*
Chinese Academy of Sciences, Beijing, 100190, China
[8]*Department of Physics, Kyoto University, Kyoto 606-8502, Japan*
[9]*Shanghai Synchrotron Radiation Facility, Shanghai Advanced Research Institute,*
Chinese Academy of Sciences, 201204 Shanghai, China
[10]*School of Physics and Astronomy, Shanghai Jiao Tong University, Shanghai 200240, China*
[11]*Zhangjiang Institute for Advanced Study, Shanghai Jiao Tong University, Shanghai 200240, China*

Quantum many-body systems, particularly, the ones with large near-E_F density states, are well known for exhibiting rich phase diagrams as a result of enhanced electron correlations. The recently discovered locally noncentrosymmetric heavy fermion superconductor $CeRh_2As_2$ has stimulated extensive attention due to its unusual H-T phase diagram consisting of two-phase superconductivity, antiferromagnetic order, and possible quadrupole-density wave orders. However, the critical near-E_F electronic structure remains experimentally elusive. Here, we provide this key information by combining soft-x-ray and vacuum ultraviolet (VUV) angle-resolved-photoemission-spectroscopy measurements and atom-resolved density-functional-theory (DFT) $+ U$ calculations. With bulk-sensitive soft x ray, we reveal quasi-2D hole and electron pockets near the E_F. On the other hand, under VUV light, the Ce flat bands are resolved with the c-f hybridization persisting up to well above the Kondo temperature. Most importantly, we observe a symmetry-protected fourfold Van Hove singularity (VHS) coexisting with the Ce $4f_{5/2}^1$ flat bands at the X point, which, to the best of our knowledge, has never been reported before. Such a rare coexistence is expected to lead to a large density of states at the zone edge, a large upper critical field of the odd-parity phase, as well as spin and/or charge instabilities with a vector of $(1/2, 1/2, 0)$. Uniquely, it will also result in a new type of f-VHS hybridization that alters the order and fine electronic structure of the VHS and flat bands. Our findings provide not only key insights into the nature of multiple phases in $CeRh_2As_2$ but also open up new prospects for exploring the novelties of many-body systems with f-VHS hybridization.

Subject Areas: Condensed Matter Physics,
Strongly Correlated Materials,
Superconductivity

*These authors contributed equally to this work.

†Corresponding author: yanase@scphys.kyoto-u.ac.jp

‡Corresponding author: baiqing@sjtu.edu.cn

§Corresponding author: huangyaobo@sari.ac.cn

I. INTRODUCTION

In correlated electron systems, due to the interplay of charge, lattice, spin, and orbital degrees of freedom, multiple orders exist with close energy, temperature, or timescales. Understanding and engineering these different orders has always been the major theme of condensed matter physics. One important aspect is the electronic structure near the Fermi energy (E_F). It is generally

believed that a large density of states (DOS) can enhance the many-body interactions and prompt novel correlated phenomena like new phases of matter.

Van Hove singularity (VHS), usually characterized by extrema and saddle points in the band structure, is arguably the most common source of large DOS for low-dimensional systems. More importantly, it appears to play a major role in controlling the interplay among different orders, including superconductivity, and spin- and charge-density waves [1–3]. One of the most famous examples is cuprates [1,4–15], where VHS is proposed to be responsible for many intriguing transport phenomena, such as the strange metal phase and the anomalous isotope effect [13–15]. Second, recent strain-dependent studies have found that the T_c of Sr_2RuO_4 reaches a maximum when the saddle point crosses E_F [16]. Third, VHS is also observed in iron-based superconductor KFe_2As_2 and is interpreted as the main driving force for many surprising properties like a nodal gap and large normal-state Sommerfeld coefficient [17]. Fourth, the recently discovered kagome superconductor is also characterized by a VHS near the E_F, and it certainly plays a vital role in the competing of superconducting and charge order [18–20]. In addition, a recent theoretical work predicts that when the E_F of graphene is doped to the VHS, chiral superconductivity can be induced, opening the door for graphene-based topological superconductors and Majorana fermions [21]. Last but not least, very recently, Luckin *et al.* reported the controlling of charge-density wave orders in $2H - TaSe_2$ using a VHS [22]. It has been increasingly clear that VHS provides a paradigm for the elucidation of the role of large DOS and enhanced electron correlations on the low-energy physics of super-conducting materials.

In parallel with VHS, the flat band is another well-known trigger of strong electron correlations [23]. A prototypical example is heavy fermion materials, where the interplay between mostly localized $4f$ flat bands and itinerant conduction bands gives rise to a multitude of extraordinary correlated phenomena, including but not limited to, unconventional superconductivity, Kondo resonance, heavy fermion quasiparticles, magnetic order, hidden order, non-Fermi-liquid ground states, and quantum critical phenomena [24]. Recently, the locally noncentrosymmetric heavy fermion superconductor $CeRh_2As_2$ has attracted much attention [25–50]. Apart from the Kondo c-f electron-band hybridization, it exhibits the following peculiarities: (i) The most striking feature is the c-axis field-induced two-phase superconductivity SC1 and SC2, as illustrated in Fig. 1 [25,43]. As we know, multiphase unconventional superconductors are rare in nature. $CeRh_2As_2$ stands out not only because of the existence of the SC1 and SC2 phases but also due to the odd-parity nature of SC2, providing a feasible platform for realizing topological crystalline superconductors and Majorana fermions [38,48,51]. It is also worth highlighting that the
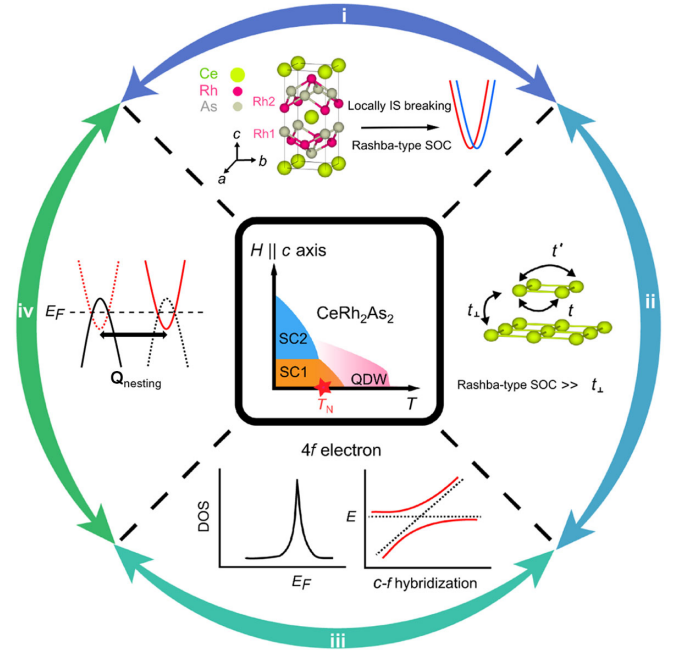

FIG. 1. Schematic H-T phase diagram of $CeRh_2As_2$. The phase transition between two superconducting phases has been observed with the H$\parallel c$ axis. Slightly above T_c, another QDW phase occurs and persists into the superconducting state shown in the pink area. Slightly down T_c, an AFM order with an odd-parity multipole has been revealed by NQR experiments labeled by a red star. (i) The crystal structure of $CeRh_2As_2$ generated by Vesta [54]. (ii) Schematic illustration of the bilayer Rashba-Hubbard model. Yellow circles represent the Ce atoms of $CeRh_2As_2$. The first- and second-neighbor intralayer- and interlayer-hopping integrals are t, t', and $t_\perp$. (iii) Schematic illustration of large DOS of Ce $4f$ electrons near the Fermi level (left) and the c-f hybridization within the periodic Anderson model (right). (iv) Schematic drawing of the energy-band nesting connected by a wave vector $Q_{nesting}$.

corresponding upper critical field of SC2 is up to 14 T, well exceeding the Pauli-limiting field of BCS superconductors. (ii) Slightly above T_c, another nonmagnetic order occurs and persists into the superconducting state. Such a coexisting order was interpreted as a quadrupole-density wave (QDW) [26]. (iii) Surprisingly, recent nuclear-quadrupole-resonance (NQR) experiments revealed an antiferromagnetic (AFM) order with an odd-parity multipole inside the superconductivity phase [27,29], beyond our conventional wisdom of superconductivity and magnetism, where the coexistence has been observed only when $T_N > T_c$ [52,53]. Finally, all of these coexisting phases emerge from a non-Fermi-liquid state below 4 K, indicating the proximity to a quantum critical point [25].

The above results demonstrate a rare coexistence of a f-electron flat band, two-phase superconductivity, odd-parity magnetic multipole, and putative QDW in $CeRh_2As_2$. Theoretically, the unique crystal and near-E_F electronic structures are believed to be the main driving force [33,36,37,40,41,46,55–57] of these phenomena.

As illustrated in Fig. 1, CeRh$_2$As$_2$ crystallizes in the CaBe$_2$Ge$_2$-type tetragonal structure with space group $P4/nmm$ [58]. It consists of vertical-stacking 2D Ce layers and Rh$_2$As$_2$ blocks. Notably, the Ce layer is located between two inequivalent Rh$_2$As$_2$ blocks (i.e., Rh-As-Rh and As-Rh-As). Therefore, the inversion symmetry is locally broken at the Ce sites, while the global inversion symmetry is still maintained with the inversion center in the middle of the two Ce atoms. The locally noncentrosymmetric crystal structure and the consequent Rashba spin-orbit coupling (SOC), which is larger than the interlayer hopping as a result of large near-edge DOS, are crucial for the AFM order and the field-induced parity transition [33,36,37,39,41,46]. On the other hand, the pronounced nesting features of the Fermi surfaces play an essential role in stabilizing QDW order [26]. It has been increasingly clear that the near-E_F electronic structure is the key ingredient for clarifying the rich phases in CeRh$_2$As$_2$. However, the momentum-resolved band structure so far remains elusive experimentally. In particular, angle-resolved-photoemission-spectroscopy (ARPES), scanning tunneling microscopy (STM), and quantum oscillation measurement have not been reported.

In this work, we present the first report on the band structure from a combination of bulk-sensitive soft-x-ray and resonant vacuum ultraviolet (VUV) ARPES. Uniquely, we unravel a VHS at the Brillouin-zone (BZ) edge X point, hybridizing with the $4f_{5/2}^1$ bands in the vicinity of the E_F. Our study raises new possibilities of interplay between large-density flat bands and VHS, offering an important dimension for how these hybridizing electrons entangle in various symmetry-broken phases.

II. RESULTS

We first investigated the bulk-electronic structure by performing systematic soft-x-ray ARPES measurements on the (001) surface. The employment of soft x rays improves both the bulk sensitivity and the intrinsic k_z resolution, allowing the accurate navigation of the bulk bands in the 3D BZ by photon-energy-dependent measurements. Indeed, the measured constant-energy map in the vertical Γ-M-Z-A plane exhibits a weak modulation along the k_z direction with a period of $2\pi/c$ [Fig. 2(a)], where c is the lattice constant, confirming their bulk nature. Figures 2(b) and 2(c) display the measured constant-energy plots within the $k_z = 0$ plane at binding energy of $E_B = 0$ and -0.4 eV, respectively. One can directly identify one squarelike hole pocket centered at the Γ point (indicated by red dots) and one nearly diamondlike electron pocket centered at the M point (indicated by white dots) labeled as α and β, respectively. These two pockets are further evidenced by the subsequent high-precision photoemission intensity [Fig. 2(d)], curvature [Fig. 2(e)], and momentum distribution curves (MDCs) [Fig. 2(f)] plots along the Γ-M

direction, as highlighted by red and white (black) arrows. Note that the β pocket is mainly resolved in the second BZ.

Similarly, at the $k_z = \pi$ plane, Figs. 2(g) and 2(h) also exhibit one hole (labeled as α') and one electron pocket (labeled as β') near the E_F. In addition, Figs. 2(g) and 2(h) clearly show another electron pocket surrounding the Z point in the second BZ labeled by γ'. Actually, taking a close look at Fig. 2(e), one can recognize a similar electron pocket centered at the Γ point, as also evidenced by the enhancement of the MDC intensity in Fig. 2(f). The existence of the γ pocket is further supported by density-functional-theory (DFT) calculations, which will be discussed later. In short, with bulk-sensitive soft-x-ray ARPES measurements, we mainly observed three types of bulk Fermi pockets near the E_F, i.e., $\alpha(\alpha')$, $\beta(\beta')$, and $\gamma(\gamma')$. By fitting the peak location of MDCs with the Lorentzian function, we further extracted the band dispersions of these pockets, as summarized in Figs. 2(k) and 2(l). Comparing Fig. 2(k) with 2(l), one can see that α and β closely resemble α' and β'. Consistently, Fig. 2(a) shows a very weak dispersion of these two pockets along the k_z direction, affirming their quasi-2D nature.

More importantly, as proposed by Ref. [26], the nesting of electron and hole Fermi surfaces at the $k_z = 0$ and $k_z = \pi$ plane is crucial for the formation of the novel QDW order. Here, from Figs. 2(k) and 2(l) one can come up with two possible imperfect nesting instabilities. One possibility is the nesting between the $\alpha(\alpha')$ and $\beta(\beta')$ pockets, giving rise to a nesting vector q_1 of approximately $(1/2, 1/2, 0)$. The other possibility is the nesting between the $\alpha(\alpha')$ and $\gamma(\gamma')$ pockets, resulting in a small in-plane vector q_2. X-ray or neutron-scattering measurements are ideal tools to examine the above nesting instabilities.

Moving on to the Fermi surface near the X point, we present the high-resolution ARPES intensity plots in Figs. 3(a) and 3(b) and corresponding curvature plots in Figs. 3(c) and 3(d) along the two perpendicular directions passing through X point. Whereas Figs. 3(a) and 3(c) show an electronlike band bottom centered at the X point, a holelike band is observed along the X-M direction. Consistently, the electron bottom shifts down instead of up as one moves the cut along the high-symmetry-line Γ-X direction [Fig. 3(g)]. These observations directly demonstrate the existence of a VHS at the X point, as illustrated in Fig. 3(g). To precisely determine the energy location of the VHS, we fitted the peak positions of the energy distribution curves (EDCs) along both Γ-X and X-M directions with the spline background subtracted in Figs. 3(e) and 3(f). The VHS was found at a binding energy of approximately 75 meV $\pm$ 60 meV, where the error bar represents half FHWM of the Gaussian fitting [59]. Such a near-E_F VHS is anticipated to contribute to the exotic phenomena in CeRh$_2$As$_2$.

To further understand the near-E_F states and the VHS, we performed systematic orbital- and atom-resolved
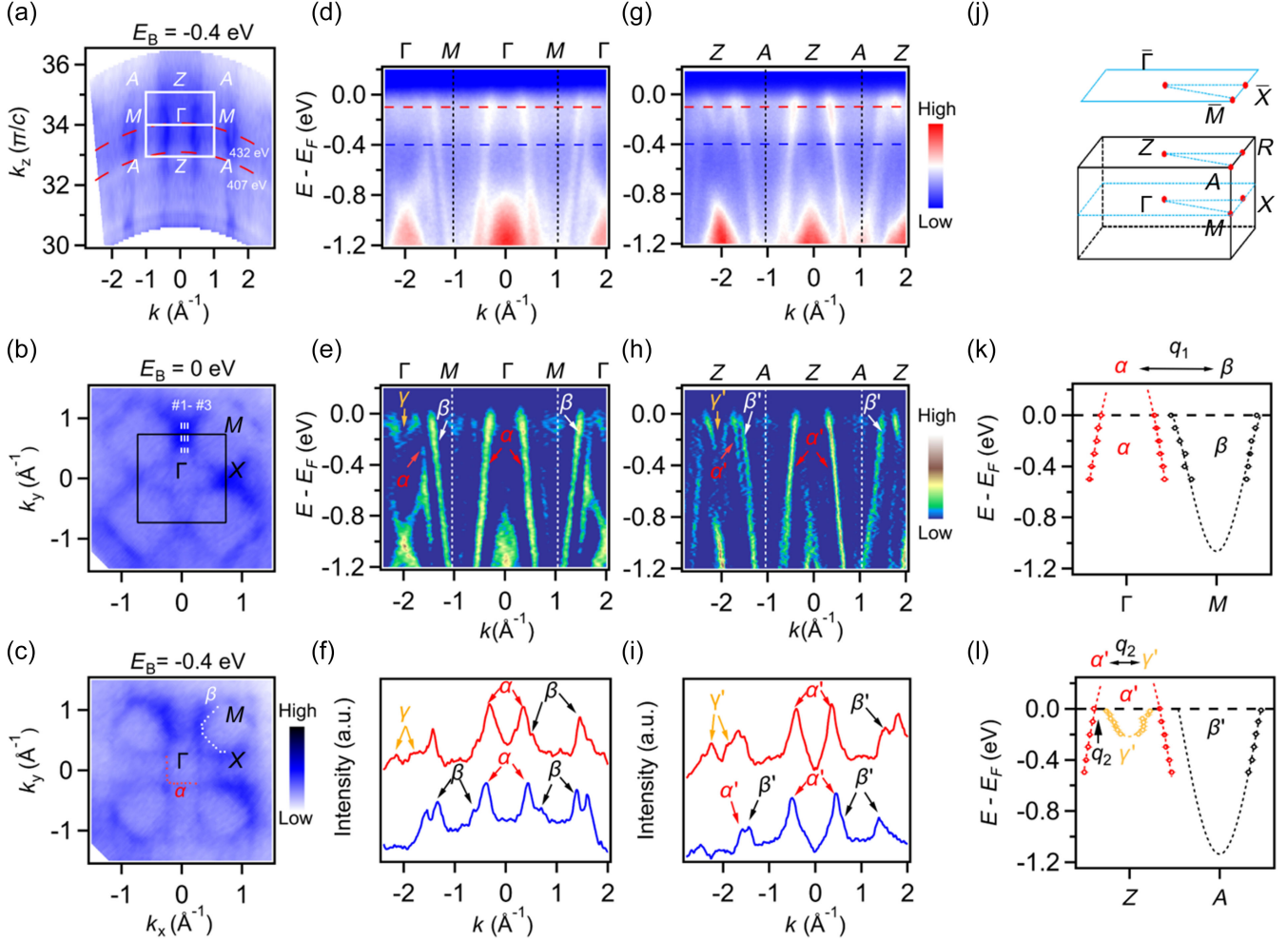
FIG. 2.   Overall electronic structure of CeRh$_2$As$_2$. (a) ARPES constant-energy map collected in the vertical Γ-M-Z-A plane with $E_B = -0.4$ eV in a range of photon energies from 350 to 510 eV. The inner potential $V_0 = 16.5$ eV and the lattice constant $c = 9.8616$ Å. (b),(c) Constant-energy map in the Γ-M-X plane at $E_B = 0$ and $E_B = -0.4$ eV, respectively. (d),(e) ARPES and curvature intensity plots along the high-symmetry-line Γ-M direction. (f) The corresponding MDCs along the Γ-M direction. The red and blue lines are taken at $E_B = -0.1$ eV and $E_B = -0.4$ eV, respectively [indicated in (d)]. (g)–(i) Same as (d)–(f) but along the Z-A direction. (j) Three-dimensional bulk BZ and the projected (001) surface BZ of CeRh$_2$As$_2$ with high-symmetry points indicated. (k),(l) Summary of the band dispersions along the Γ-M and Z-A directions, respectively. Bands $\alpha(\alpha')$, $\beta(\beta')$, and γ' are extracted by fitting the peak positions of MDCs with Lorenzian functions. All data were taken on the (001) surface at 20 K with linear horizontal (LH) polarization (within the incident plane).

DFT + U calculations. The calculated band structures, in good agreement with the previous DFT and DFT + DMFT (dynamical mean-field theory) reports [49] (see Appendix B for further details), are summarized in Figs. 4(a) and 4(b). Comparing the calculated band structure with the experimental data, we came to the following conclusions. First of all, the calculated electronic structure, especially the one with U = 2 eV, is generally consistent with the ARPES results, as evidenced by Figs. 4(c) and 4(d). Specifically, the correspondence of the observed near-E_F $\alpha(\alpha')$, $\beta(\beta')$, $\gamma(\gamma')$ bands is marked by red letters in Fig. 4(b). Note that from the calculated band structure, each $\alpha(\alpha')$, $\beta(\beta')$, or $\gamma(\gamma')$ actually represents a pair of closely spaced bands. These band doublets are not resolved in Fig. 2 limited by the energy

and momentum resolution of soft x rays. Second, one can identify several VHSs at the X point [as marked by red arrows in Fig. 4(b)], and these VHSs are fourfold Dirac nodal points protected by the nonsymmorphic glide symmetry [60]. In other words, the VHSs are robust against crystal-symmetry-preserved perturbations. Third, comparing the calculated band structure without and with SOC in Figs. 4(a) and 4(b), one realizes that the SOC-induced band splitting is best seen at the BZ edge, such as the near-E_F bands in the X-M and R-A directions, as highlighted by blue dash circles. While our ARPES measurements cannot access these bands above E_F, we resolved two-hole bands that are dominated by the two nonequivalent Rh atoms, as pointed out by the white arrows in Fig. 4(d), further
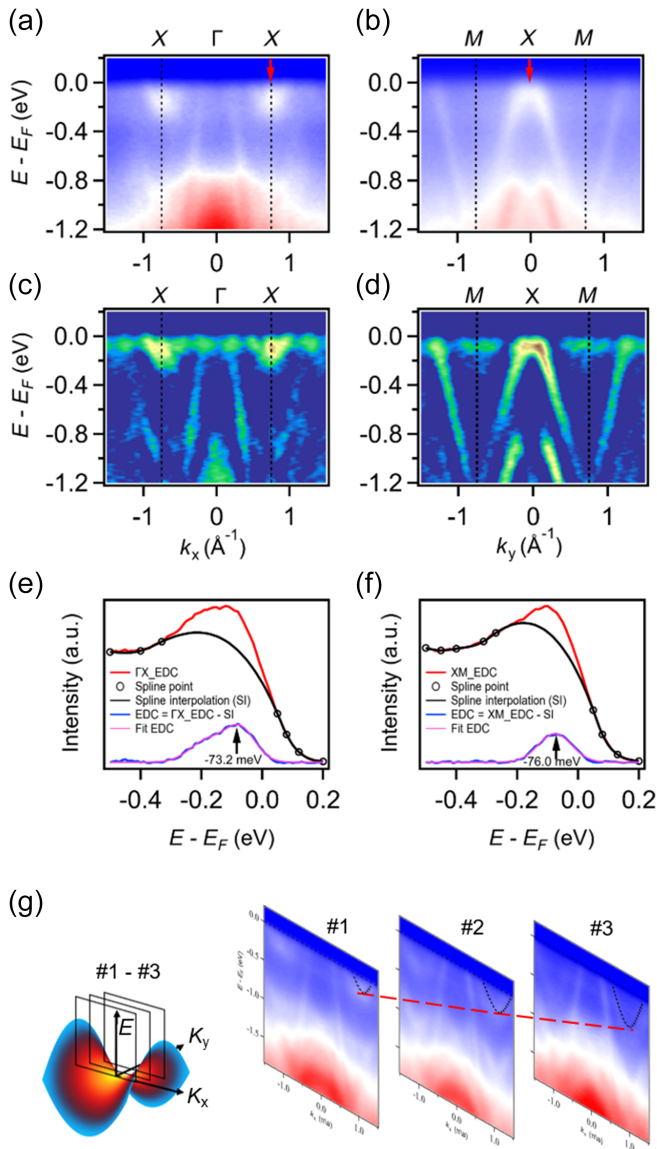
FIG. 3. VHS at the X point. (a),(b) High-precision photoemission intensity plots along the Γ-X and X-M directions, respectively. (c),(d) The corresponding curvature intensity plots. (e),(f) Fitting of the EDCs extracted from the ARPES spectrum in (a), and (b) at Γ and X, respectively. (g) Schematic diagram of VHS and ARPES intensity plots along cuts 1–3, whose momentum locations are indicated by the white dashed lines in Fig. 2(b). All data were taken on the (001) surface at 20 K with LH polarization.

confirming the lack of local inversion symmetry at the Ce sites. Last but not least, although the calculated electronic structure generally matches the ARPES data, there are still some notable discrepancies in band dispersions or Fermi surfaces (see Appendix B for further details). For example, the measured $\alpha(\alpha')$ bands cross E_F, while they are not in Fig. 4(b). Similarly, the measured VHS is much closer to the E_F compared to Fig. 4(b). These differences suggest extra hole doping of the measured sample or

additional band renormalizations due to interactions such as Kondo hybridization.

One hallmark of heavy fermion materials is Kondo coherence and hybridization at low temperatures [61–70]. Specifically, in CeRh$_2$As$_2$, the Kondo coherence has been hinted by a broad maximum in resistivity at a temperature $T^* \sim 40$ K [25]; however, direct spectroscopic evidence has been lacking. To visualize the Kondo behavior, we conducted detailed temperature-, and photon-energy-dependent VUV ARPES measurements. As shown in Fig. 5(a), the ARPES spectrum taken at 20 K and near the $4d-4f$ resonance photon energy (approximately 121 eV) shows two flat features around binding energies of -0.25 and 0 eV, providing direct evidence for the existence of $4f_{7/2}^1$ and $4f_{5/2}^1$ resonant peaks, respectively, as expected for Ce-based Kondo systems [61–66]. In addition, a broader resonant peak was resolved at a deeper binding energy of approximately -1.5 eV [Fig. 11(c)], confirming the existence of a $4f^0$ flat band. It is worth mentioning that the $4f_{7/2}^1$ and $4f_{5/2}^1$ flat bands are visible in a wide photon-energy range ranging from 90 eV to more than 200 eV (see more details in Appendix C), in contrast to many other Ce-based heavy fermion materials, where the $4f$ flat bands are typically visible in a narrower photon-energy range near the resonance energy.

Moving to the Kondo c-f hybridization, the measured flat bands exhibit clear enhancement of spectral intensity near the crossing points of the conduction α band [highlighted by red arrows in Fig. 5(a)], signifying the c-f electron band hybridization. The hybridization is better illustrated by the corresponding coherence peaks in the EDCs and the corresponding spectra weight, as shown in Figs. 5(b) and 5(c). Interestingly, our temperature-dependent measurements showed that the coherence peak persists up to more than 95 K. This indicates that the localized-to-itinerant transition in CeRh$_2$As$_2$ happens at a much higher temperature than T^*, as also demonstrated by recent optical conductivity measurements [28].

It should be cautioned that the surface and bulk states may exhibit different Kondo behaviors due to the termination effect and change of the crystal electric field [63–66]. Specifically, from the locally noncentrosymmetric crystal structure of CeRh$_2$As$_2$, four types of surface terminations can be induced after cleavage (see Appendix D for more details). However, in reality, our position- and sample-dependent VUV ARPES measurements did not show clear signatures of terminations effects and surface states (see more details in Fig. 13 of Appendix D). Instead, by comparing the measured VUV spectra with the soft x-ray ones, we found that the VUV spectra are also mainly contributed by bulk bands. Therefore, it is reasonable to associate Fig. 5 with bulk Kondo behavior. To be more convincing, we further performed T-dependent
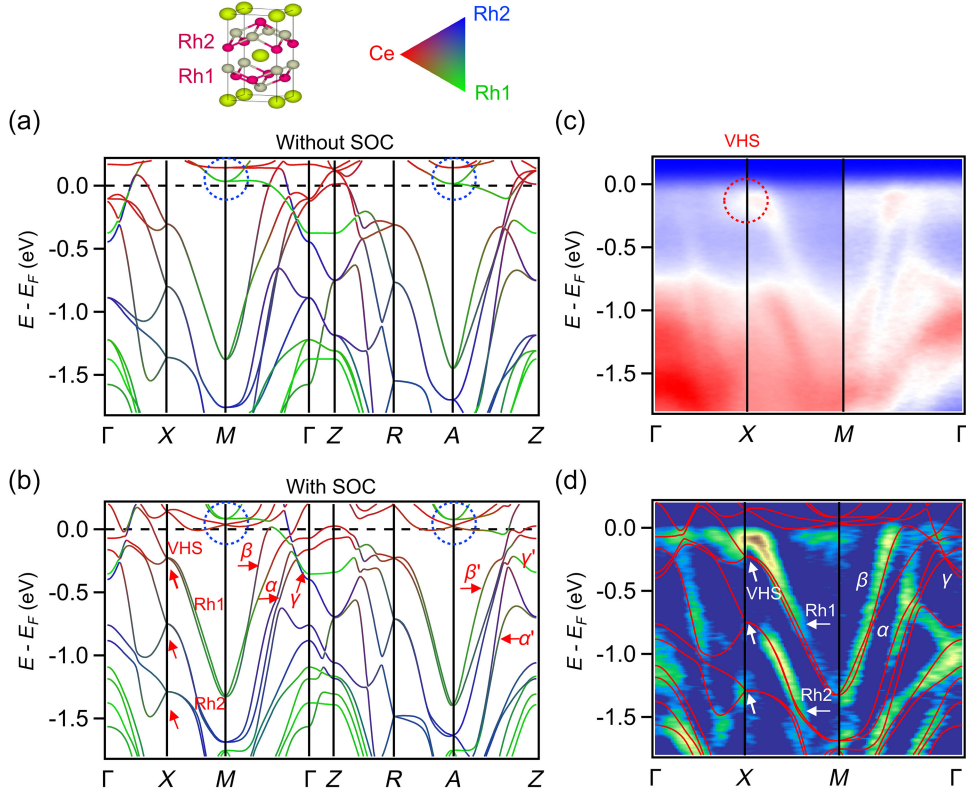
FIG. 4.   (a),(b) Band dispersion obtained by atom-resolved DFT $+ U$ calculations for U $= 2$ eV without SOC and with SOC, respectively. (c),(d) ARPES and curvature intensity plots along the Γ-X-M-Γ direction. For comparison, the corresponding calculated band structure is superposed on the experimental data in (d). All ARPES data were taken on the (001) surface at 20 K with LH polarization.
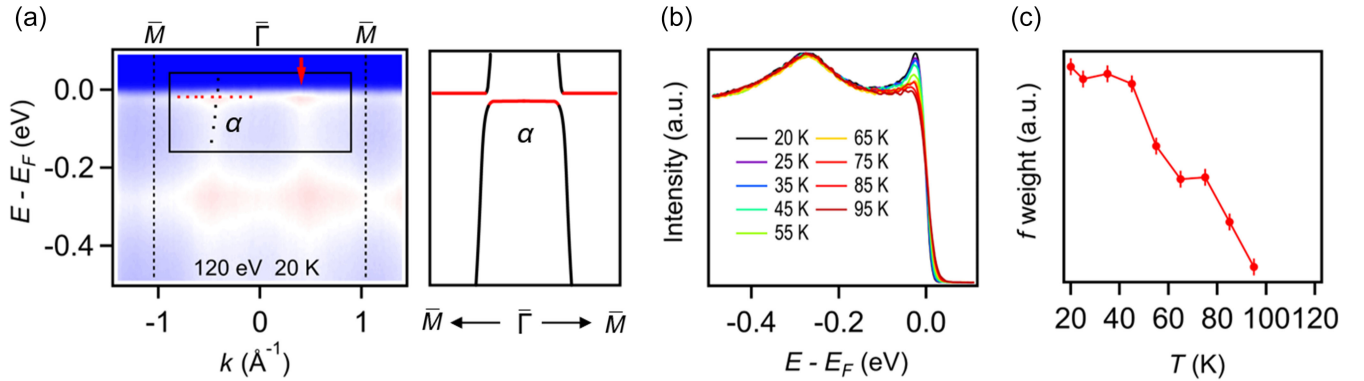

FIG. 5.   Temperature evolution of the electronic structure of $CeRh_2As_2$. (a) Left: ARPES intensity plot along $\bar{\Gamma} - \bar{M}$ at the labeled photon energy and temperature. Right: schematic illustration of the hybridization between a $4f$-electron flat band (red) and a conduction band (black) corresponding to the black rectangle area in the left panel. (b) Temperature dependence of the EDCs indicated by red arrows in (a). (c) Temperature dependence of the quasiparticle spectral weight near E_F, integrated over $(E_F - 100$ meV, $E_F + 10$ meV) in (b). Panel (a) was taken with nonpolarized light.

measurements near the other bulk bands like the bulk-electron γ pocket, and similar temperature evolution was observed (see Appendix E for more details). This consistency further demonstrates that the observed Kondo hybridization is mainly contributed by bulk bands.

III. DISCUSSION

Taken together, our soft-x-ray and VUV ARPES results show the rare coexistence of symmetry-protected fourfold VHS and f-electron flat bands in $CeRh_2As_2$, as summarized in Fig. 6(a). To the best of our knowledge, such a
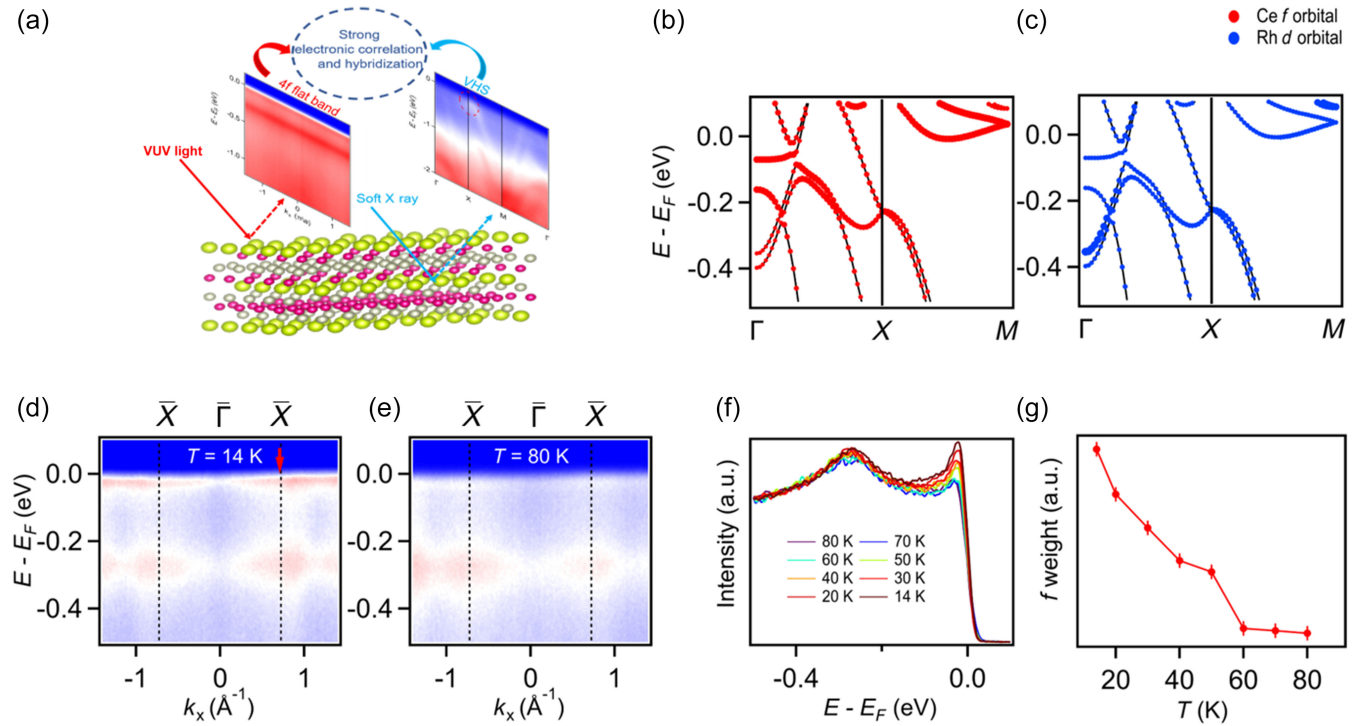
FIG. 6. Interaction between VHS and a $4f$ electron. (a) Summary of the interaction between VHS and a $4f$ flat band. (b),(c) Orbital-projection band-structure calculation of CeRh$_2$As$_2$ along the Γ-X-M direction with SOC. (d),(e) ARPES intensity plots along $\bar{\Gamma} - \bar{X}$ taken with 140 eV LH-polarized light at 14 and 80 K, respectively. Note that the lack of center intensity is caused by the failure of the MCP channel in the analyzer. (f) Temperature dependence of the EDCs at the Fermi crossings of the $\bar{X}$ point labeled by a red arrow in (d). (g) Temperature dependence of the quasiparticle spectral weight in the vicinity of the $\bar{X}$ point integrated over ($E_F - 100$ meV, $E_F + 10$ meV) in (f).

coexisting has not been reported, and CeRh$_2$As$_2$ thus provides a unique platform to study the relationship between the flat-band, symmetry-protected VHS, and multiple broken-symmetry states. Particularly, our observation provides key information for elucidating the long-sought low-energy excitations and the novel two-phase superconductivity. First of all, generally speaking, the flat band and VHS give rise to a large DOS, which implies that more electrons contribute to the low-energy excitations. As a consequence, many-body interactions are enhanced, leading to a multitude of competing or coexisting phases, as evidenced by cuprates, heavy fermions, and the recently discovered moiré superconductors [71–73]. In this regard, it is reasonable to ascribe the two superconducting phases in CeRh$_2$As$_2$ to the coexistence of a flat band and VHS in a locally noncentrosymmetric crystal structure. Indeed, the absence of unconventional superconductivity in LaRh$_2$As$_2$ confirms the crucial role of f-electron correlation in driving the unconventional superconductivity [74]. Besides the enhanced electron correlations, it has been recognized that a large orbital limit of the critical field H_{c2}^{orb} is essential for the observed two-phase superconductivity in CeRh$_2$As$_2$ [75]. Theoretically, $H_{c2}^{\mathrm{orb}} = \phi_0/(2\pi\xi^2)$, $\xi = v_F/T_c$. Therefore, the small v_F of both the flat band and VHS naturally leads to large H_{c2}^{orb}. Another essential

aspect is the VHS-induced large DOS at the BZ edge that is also proposed to enhance the effect of Rashba splitting. Moreover, the observation of quasi-2D electron and hole pockets indicates that the interlayer hopping is small. This comparison demonstrates that the Rashba SOC is larger than the interlayer hopping in CeRh$_2$As$_2$, which is crucial for the AFM order and the field-induced parity transition in the superconducting state [33,36,37,39,41,46,56]. The above three clues demonstrate that the coexistence of a flat band and fourfold VHS is responsible for the observed large critical field and the even-to-odd-parity transition in CeRh$_2$As$_2$.

Apart from stabilizing an odd-parity superconducting state, the presence of VHS leads to divergence of the susceptibilities at a wave vector that connects two VHSs [76], pointing toward the formation of charge, spin, and higher-order multipole instabilities. More specifically, the two saddle points at the X point can be connected via a wave vector of $q_3 = (1/2, 1/2, 0)$, as indicated by the black arrow in Fig. 10(a) in Appendix B. Meanwhile, as shown in Figs. 2(k) and 2(l), the observed $\alpha(\alpha')$ and $\beta(\beta')$ pockets as well as the $\alpha(\alpha')$ and $\gamma(\gamma')$ pockets could be imperfectly nested by q_1 of approximately $(1/2, 1/2, 0)$, a small in-plane vector $q_2 = \tau$, respectively. Since $q_1 \sim q_3$, it is reasonable to ascribe them as the main trigger for the
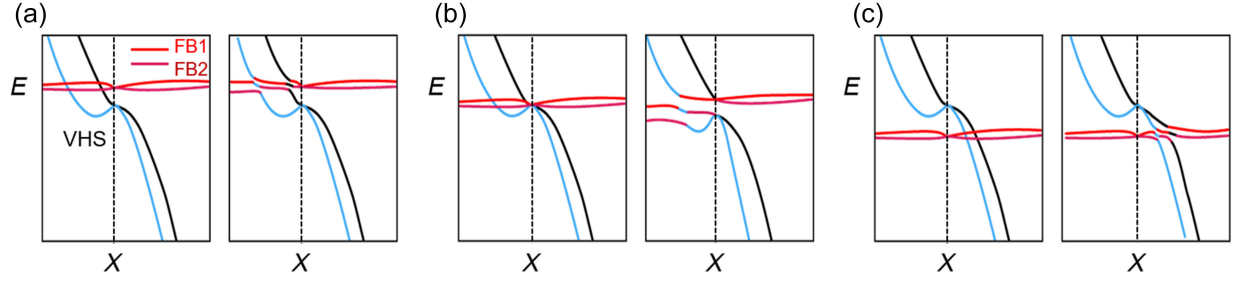
FIG. 7. (a)–(c) Schematic band structure for a possible f-VHS unhybridized and hybridized case in CeRh$_2$As$_2$ when the $4f$ flat bands are located above, exactly at, and below the VHS, respectively. Red lines illustrate nearly flat f-electron bands, and blue and black lines show conduction Dirac bands with VHS. Note that there should be two bands for both conduction electrons and f-electrons because of the sublattice degree of freedom in locally noncentrosymmetric systems. Band degeneracy at the X point is protected by nonsymmorphic space-group symmetry.

observed QDW order in CeRh$_2$As$_2$ [26,27]. Furthermore, given the fact that q_1 is an imperfect nesting vector, we believe that the VHS-driven q_3 plays a leading role. It is worth mentioning that a recent neutron-scattering experiment does report the observation of quasi-2D magnetic excitation exactly at $(1/2, 1/2)$, evidencing the existence of q_3 [77].

Importantly, our findings open a new avenue for investigating the interplay between large-DOS flat band and symmetry-protected fourfold VHS, both theoretically and experimentally. Figures 6(b) and 6(c) show the calculated orbital character of the near-E_F bands ($4f$ electrons are included and treated as valence electrons in the DFT calculations), one can clearly see that the VHS is composed of both a Ce $4f$ orbital ($j_z = \pm 3/2$) and a Rh $4d$ orbital (d_{zx+yz}, d_{xy}), providing strong theoretical evidence for the f-VHS hybridization. To experimentally verify the f-VHS hybridization, we performed systematic temperature-dependent ARPES measurements focusing on the band features near the $\bar{X}$ point [shown in Figs. 6(d)–6(g)]. Again, the apparent enhancement of spectral intensity at the $\bar{X}$ point and the corresponding coherence peak in the EDCs directly verify f-VHS hybridization at low temperatures.

Note that the details of f-VHS hybridization are beyond the current resolving power of ARPES measurements. Here, we offer some insights from a theoretical point of view. As illustrated in Fig. 7 compared to conventional c-f hybridization in Fig. 1, f-VHS hybridization has much richer consequences: (i) It leads to the transition to a higher-order VHS [78]; (ii) it also alters the low-energy excitation near the symmetry-protected Dirac nodal line; (iii) it shifts the energy location of the symmetry-protected VHS. In addition, the application of a magnetic field, carrier doping, or pressure can lead to a Lifshitz transition at the X point, which can change the topological character of CeRh$_2$As$_2$ [38,40]. More importantly, this coexistence also provides an effective way to tune the f-VHS hybridization. As demonstrated in Figs. 7(a)–7(c), the hybridized band structure, including both VHS and flat bands, changes dramatically when the $4f$ flat bands are located above,

exactly at, and below the VHS. Inevitably, the low-energy physics and phase diagram of CeRh$_2$As$_2$ would change accordingly, and new correlated phenomena are also likely to be induced.

Besides the large DOS favoring many-body instabilities, the momentum-dependent wave function of the nearly flat band due to f-VHS hybridization is an intriguing property from the viewpoint of quantum geometry, a topic of recent interest in condensed matter physics. The momentum-dependent change of the Bloch state is characterized mathematically by the quantum geometric tensor, by which the quantum geometry of the system is described [79]. Recently, several phenomena arising from quantum geometry in many-body quantum states have been theoretically clarified [80,81], and experimental verification has been awaited. For example, it has been shown that spin-triplet pairing interaction is induced by quantum geometry, which is enhanced in topological bands [82]. In CeRh$_2$As$_2$, the Dirac nodal line at the VHS is protected by crystalline nonsymmorphic symmetry and is located near the Fermi level. Thus, the Dirac nodal line might produce spin-triplet Cooper pairs. When spin-triplet Cooper pairs are admixed with spin-singlet ones due to locally noncentrosymmetric crystal structure, the upper critical field is enhanced [83]. This is consistent with the experimental observation in CeRh$_2$As$_2$ [25]. Moreover, the effect of quantum geometry is pronounced in the flat-band systems, as has been intensively studied in recent theoretical work [84,85]. Therefore, our observation of $4f$ flat-band VHS hybridization implies that CeRh$_2$As$_2$ may be a platform manifesting quantum geometry in many-body quantum states. Tuning the band structure discussed above can also enable control of quantum geometry, which is a direction of future research.

All of the above characteristics await experimental verification. In particular, sub-kelvin and ultrahigh-resolution ARPES and STM measurements are ideal tools for resolving the fine features of f-VHS hybridization, the Lifshitz transition, as well as their interaction with the observed multiple phases in CeRh$_2$As$_2$.

IV. CONCLUSION

In conclusion, with bulk-sensitive soft-x-ray and resonant VUV ARPES, as well as atom-resolved DFT + U calculations, we present a comprehensive report on the band structure of CeRh$_2$As$_2$. Our findings are threefold: (i) By accessing the bulk band with soft x rays, we confirm the quasi-2D nature of electron and hole pockets near E_F. (ii) Taking advantage of resonant ARPES measurements, the Ce $4f^1_{7/2}$ and $4f^1_{5/2}$ resonant peaks are clearly resolved. The localized-to-itinerant transition, which manifests as hybridization between f and conduction electrons, is found to well exceed the Kondo temperature. (iii) Very importantly, for the first time, we uncover a symmetry-protected fourfold VHS coexisting with the Ce $4f$ flat bands near the E_F. Considering the large density of states in both VHS and flat bands, such an unprecedented coexistence is expected to lead to a variety of correlated phenomena, including large density at the BZ edge, a large upper critical field of the odd-parity superconducting phase, spin and/or charge instabilities, at a wave vector q_3 that connects the two VHSs. Uniquely, it leads to a new type of f-VHS hybridization that alters the order and fine electronic structure of VHS and flat bands. These peculiarities are interpreted as the main driving force of the reported novel phases, including two-phase superconductivity, AFM, and QDW. Our findings offer important perspectives for understanding the novel phase diagram of CeRh$_2$As$_2$, and it also calls for more efforts to explore the new physics arising from f-VHS hybridization.

V. METHODS

A. Sample synthesis

Single crystals of CeRh$_2$As$_2$ were grown by the Bi-flux method. The starting materials cerium, rhodium, arsenic, and bismuth were placed in an alumina crucible with a molar ratio of $1.5:2:2.1:30$, and subsequently sealed into a fully evacuated quartz tube. The crucible was heated to $1130\,°C$ for 10 h, and then slowly cooled down to $700\,°C$ for 200 h. Black single crystals were gained by spinning off the Bi flux in a centrifuge (see Appendix A for more details of sample characterization).

B. Angle-resolved-photoemission spectroscopy

High-resolution ARPES measurements were performed at the Dreamline beamline and the 03U beamline of the Shanghai Synchrotron Radiation Facility with a Scienta Omicron DA30L analyzer.

The photon energy ranged from 90 to 510 eV, and the combined (beamline and analyzer) experimental energy resolution ranged from 5 to 60 meV. The angular resolution of the DA30L analyzer was $0.1°$, which directly corresponded to the in-plane momentum resolution by Eq. (1) [86]. The beam spot at 03U and Dreamline had an approximate cross-sectional size of $15 \times 15\ \mu m^2$ and $100 \times 100\ \mu m^2$, respectively. The polarization of the ARPES experiments (illustrated in Appendix F) was indicated in the caption of the figures. The chemical potential was determined from the spectra of polycrystalline gold. Fresh surfaces were obtained by cleaving CeRh$_2$As$_2$ crystals *in situ* in an ultrahigh vacuum. The base pressure was maintained below 5.6×10^{-11} Torr, and the pressure was below 1×10^{-10} Torr during the temperature-dependent ARPES experiments

$$\Delta k_\parallel^f \propto \sqrt{\frac{2mE_{\text{kin}}}{\hbar^2}}\cos\theta \times \Delta\theta.$$

C. Details of the DFT calculation

We performed the DFT calculations for paramagnetic CeRh$_2$As$_2$ using the WIEN2k package [87]. We used the full-potential linearized augmented-plane-wave + local orbitals method within the generalized-gradient approximation. The Brillouin-zone sampling was performed with $16 \times 16 \times 7$ points. We chose the muffin-tin radii of 2.5, 2.34, and 2.23 a.u. for Ce, Rh, and As, respectively. The maximum reciprocal lattice vector K_{max} was given by $R_{\text{MT}}K_{\text{max}} = 8$. The spin-orbit coupling was included in all calculations except those labeled otherwise. For DFT + U, we set Hund's coupling $J = 0$ and subtracted the double-counting correlation by approximately the mean-field formula [88].

Note added. Recently, we became aware of a related VUV ARPES study of CeRh$_2$As$_2$ [89]. Consistently, clear surface termination effects were not observed, and bulk $c - f$ hybridization was found to occur at a temperature well above the Kondo temperature. We also became aware of the slablike calculation results for different surface terminations of CeRh$_2$As$_2$ [47]. The main results are summarized in Figs. 13(i) and 13(j). In the case of the surface terminated by As-Rh-As and Rh-As-Rh layers, the near-E_F surface states are usually strongly entangled with the bulk bands, making it hard to distinguish the surface states. On the other hand, under the surface terminated by Ce-Rh and Ce-As layers, one can observe couples of holelike surface states along the $X - M$ direction. However, these features are not resolved in the measured soft-x-ray spectra in Fig. 3(b), further confirming the bulk nature of both the VUV and soft-x-ray ARPES measurements in CeRh$_2$As$_2$.

APPENDIX A: SAMPLE CHARACTERIZATION

In the main text, we outlined the synthesis method for $CeRh_2As_2$. To further evaluate the quality, composition, and crystallinity of the synthesized $CeRh_2As_2$ samples, we conducted a series of tests including x-ray diffraction (XRD), energy-dispersive x-ray spectroscopy, and x-ray photoemission spectroscopy. As shown in Fig. 8(a), the sharp (0 0 L) peaks indicated our samples were of high quality. The powder XRD data was refined effectively using FullProf software, aligning with the tetragonal space group of $P4/nmm$ (no. 129) and the lattice parameters of $a = b = 4.2847$ Å and $c = 9.8402$ Å, corroborating previous reports [25,31]. The impurity peaks were identified as Bi elemental due to Bi flux adhering to the surface of single crystals. The chemical composition of $CeRh_2As_2$ was confirmed by both energy-dispersive x-ray spectroscopy and core-level photoemission measurements in Figs. 8(b) and 8(c). It can be observed that the average atomic ratio of Ce:Rh:As is close to 1:2:2 [Fig. 8(b)] and consistently, all three elements are shown in Figs. 8(b) and 8(c).

APPENDIX B: COMPARISON AMONG DFT + U, DFT + DMFT, AND THE EXPERIMENTAL DATA

In the main text, we compared the (DFT + U)-calculated band structure with the experimental data and found that there are still some notable discrepancies in band dispersions or Fermi surfaces. For example, the measured $\alpha(\alpha')$ bands crossed E_F, while they were not in Fig. 4(b). Similarly, the measured VHS was much closer to the E_F compared to Fig. 4(b). Here, we came up with two common reasons. First of all, there is always some difference between the chemical potential of the measured sample and the calculation due to crystal defects or cleaving-induced electron or hole doping. This inevitably alters the Fermi surfaces, particularly for strongly correlated systems as the k_F of the positions of renormalized heavy bands are more sensitive to chemical potential. Second, the discrepancy may also result from additional electron correlations that are missed in DFT + U calculations, such as Kondo hybridization.

One may argue that the many-body calculation combined with an *ab initio* calculation, e.g., DFT + DMFT, or Anderson's impurity model, may provide a better description of the band structure. In Figs. 9 and 10,
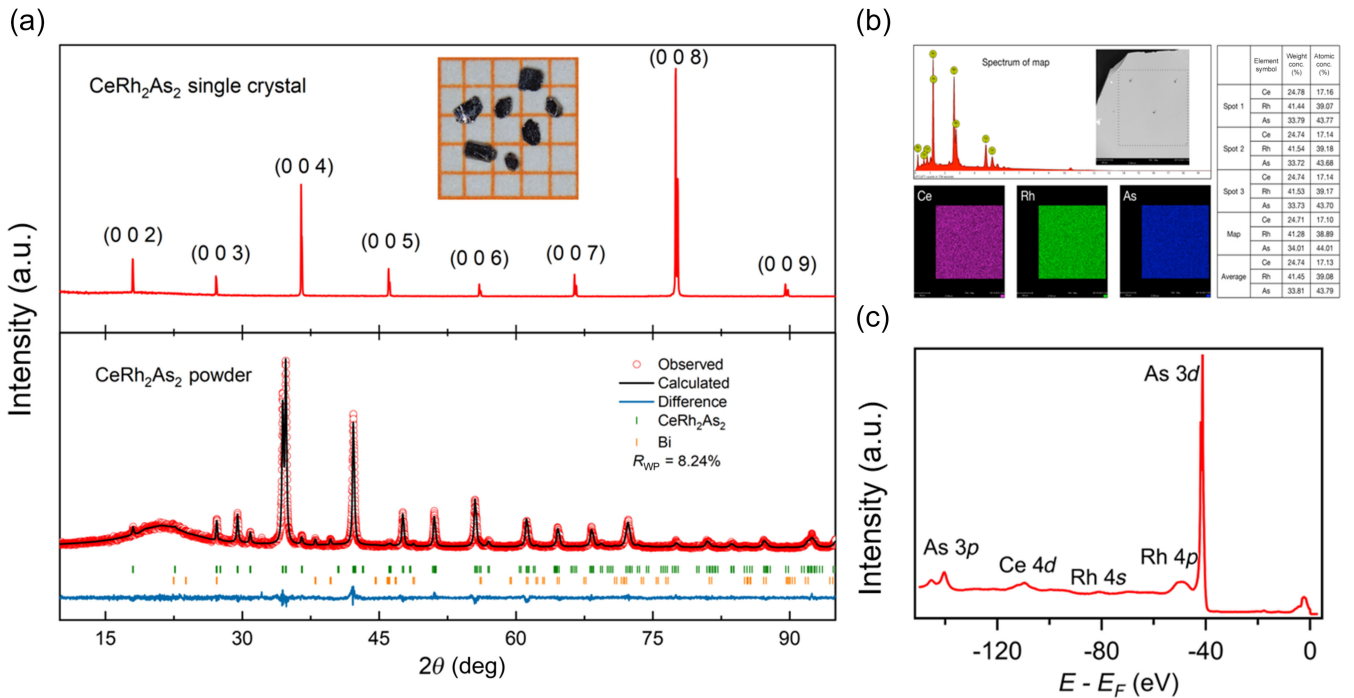

FIG. 8. (a) The x-ray-diffraction patterns of single crystal and powder of $CeRh_2As_2$. (b) Energy-dispersive x-ray spectroscopy of $CeRh_2As_2$. (c) Core-level photoemission spectroscopy of $CeRh_2As_2$ taken with $hv = 350$ eV.
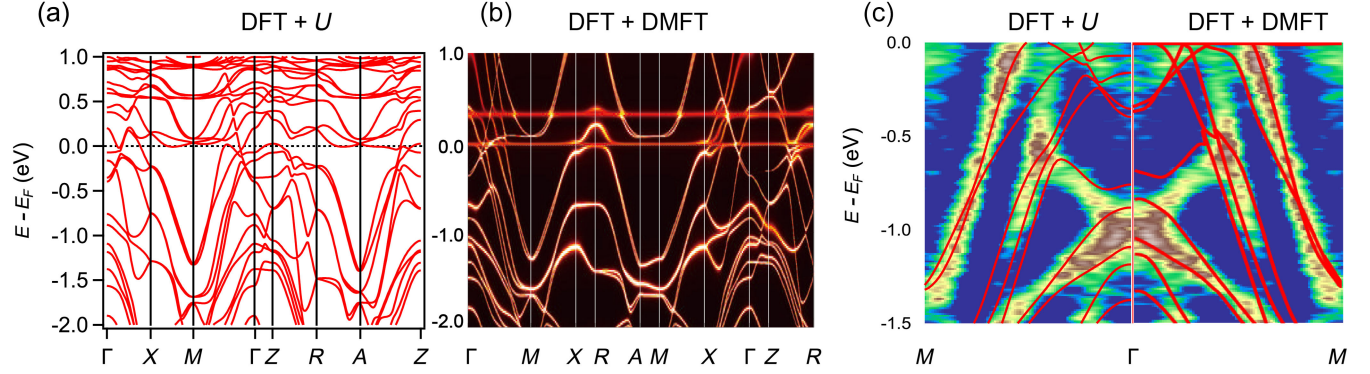
FIG. 9. (a) Band structure obtained from DFT + U. (b) Band structure obtained from DFT + DMFT adapted from Ref. [49]. (c) Comparison of our measured band structure, the DFT + U band structure, and the DFT + DMFT band structure along Γ-M direction.
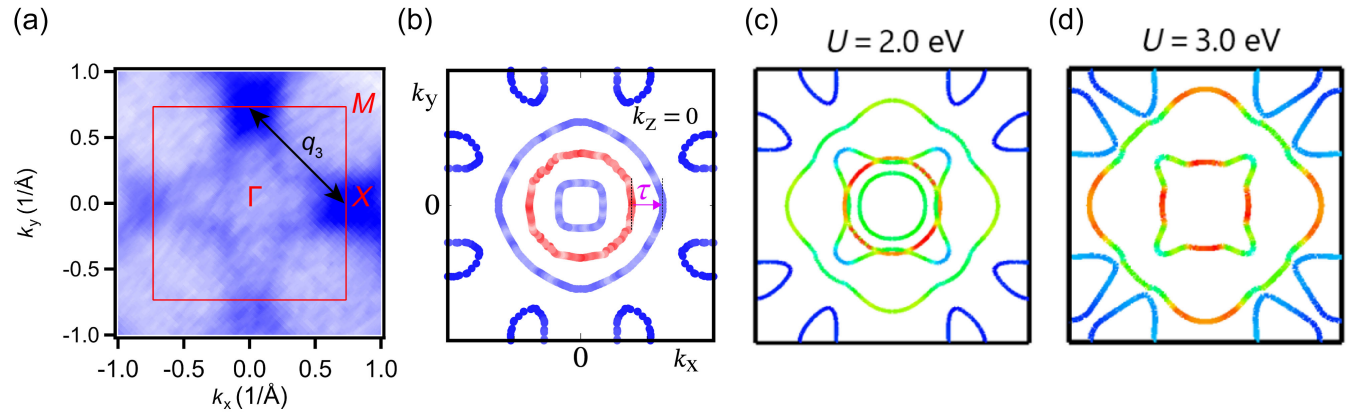

FIG. 10. (a) Fermi surface measured by ARPES experiments. The black arrow in (a) indicates the possible nesting vector q_3 that connects two VHSs at X points. (b) Fermi surface derived from the Anderson model impurity Hamiltonian adapted from Ref. [26]. (c),(d) Fermi surface obtained from the DFT + U method, $U = 2.0$ and 3.0 eV, respectively.

we further supplemented the recent DFT + DMFT results and Anderson's impurity model done by Ma *et al.* [49] and Hafner *et al.* [26], respectively.

Figures 9(a) and 9(b) summarized the (DFT + U)- and (DFT + DMFT)-calculated band structure along high-symmetry lines, and one can see that they agreed with each other well, corroborating the validity of DFT + U. To be more precise, we extracted the calculated band structure along the Γ-M direction from DFT + DMFT in Ref. [49] and compared it directly with our ARPES data and DFT + U results. Again, it can be seen that there is high consistency among DFT + U, DFT + DMFT, and measured band structure, as shown in Fig. 9(c). One arguable observation might be that DFT + DMFT reproduces the band structure near E_F slightly better than DFT + U (e.g. the calculated energy position of VHS), while the DFT + U calculation better reproduces the band structure below the E_F.

As for Anderson's impurity model, we believe that DFT + U is also compatible with it. More specifically, we found that the Fermi surfaces for $U = 2.0$ best match the Fermi surface derived from the Anderson

model impurity Hamiltonian in Ref. [26], as shown in Fig. 10. Consistently, $U = 2.0$ eV also best describes the experiential data. This consistency further rationalizes Figs. 4(a) and 4(b).

APPENDIX C: PHOTON-ENERGY-DEPENDENT ARPES MEASUREMENTS OF THE 4f FLAT BANDS

In Fig. 5(a) of the main text, we presented direct ARPES evidence of $4f_{7/2}^1$ and $4f_{5/2}^1$ states along the $\bar{\Gamma} - \bar{M}$ direction. Here, to visualize the deeper binding-energy $4f^0$ state, we supplemented the ARPES intensity plots with a wider energy range under off-resonance and on-resonance conditions. As shown in Fig. 11(a), with the off-resonance photons (115 eV), the ARPES spectrum was dominated by dispersive bulk bands, as also supported by DFT calculations. On the other hand, the Ce 4f emission was significantly enhanced with the on-resonance (120 eV) photons, as highlighted by black arrows in Fig. 11(b). More specifically, in addition to the $4f_{7/2}^1$ and $4f_{5/2}^1$ resonant peaks locating
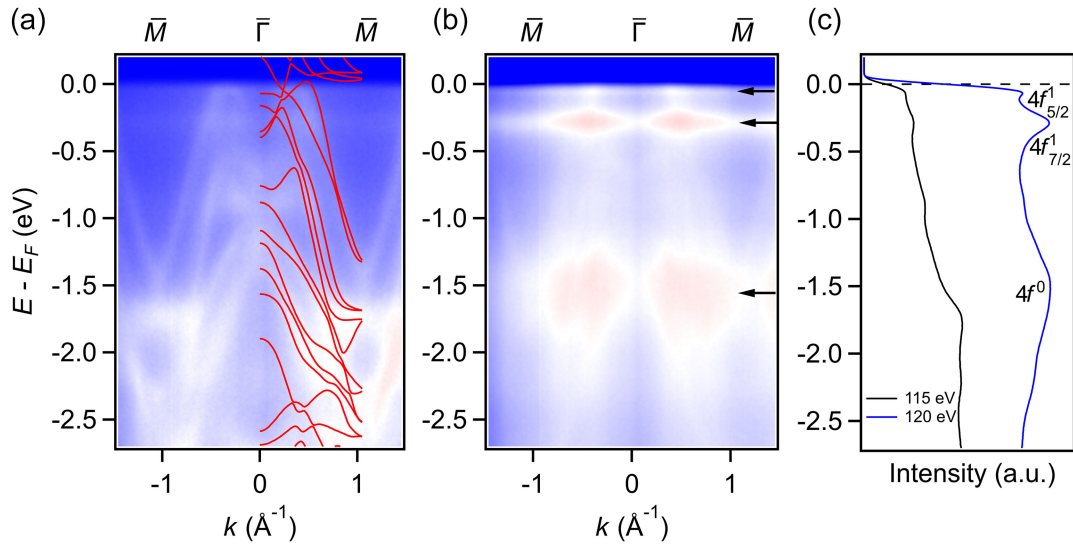
FIG. 11.   (a),(b) ARPES intensity plots along the $\bar{\Gamma} - \bar{M}$ direction taken with off-resonance (115 eV) and on-resonance (120 eV) photons, respectively. (c) The corresponding angle-integrated EDCs. The peak positions of the $4f_{5/2}^1$, $4f_{7/2}^1$, and $4f^0$ states are highlighted by black arrows in (b). All data were taken on the (001) surface at 20 K with LH polarization.

approximately -0.25 and 0 eV, respectively, the measured integrated EDC [blue curve in Fig. 11(c)] showed a broader resonant peak at a binding energy of approximately -1.5 eV, affirming the existence of the $4f^0$ state.

In Fig. 5(a) of the main text, we showed the measured band dispersions along the $\bar{\Gamma} - \bar{M}$ direction at photon energies of 120 eV. Here, in Fig. 12, we supplemented the ARPES intensity plots at a wide photon-energy range
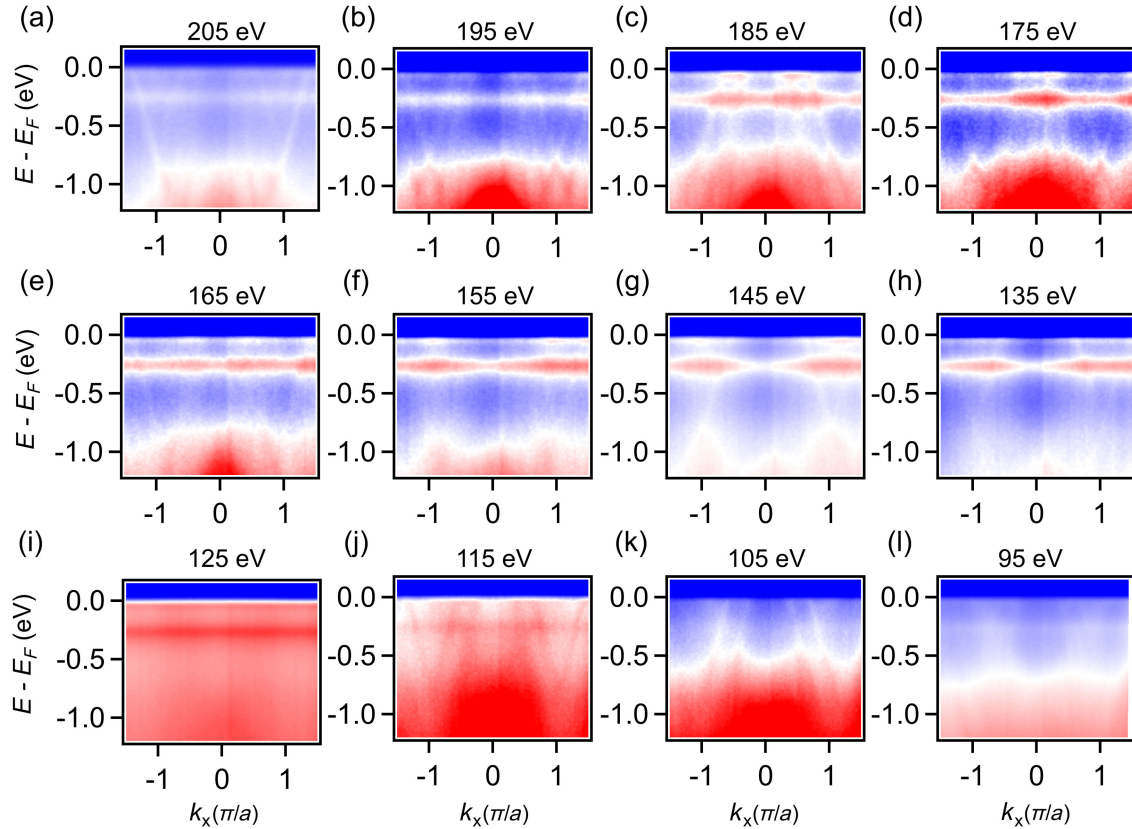

FIG. 12.   Heavy $4f$-electron flat band along $\bar{\Gamma} - \bar{X}$ at 20 K by wide-range photon-energy-dependent ARPES measurements with LH polarization.

ranging from 95 to 205 eV. Again, we observed two flat bands located at about -0.25 eV and E_F in almost all panels, providing direct evidence for the existence of $4f_{7/2}^1$ and $4f_{5/2}^1$ flat bands. Note that the measured flat bands also exhibit clear enhancement of spectral intensity at the crossing points of the conduction bands [see, e.g., Fig. 12(c)], further demonstrating the c-f hybridization.

APPENDIX D: EXPLORING SURFACE TERMINATIONS AND BULK NATURE OF CeRh$_2$As$_2$

Because of the locally noncentrosymmetric crystal structure, two possible cleavage planes can be derived, as depicted in Fig. 13(e). Correspondingly, the two cleavage planes result in four possible surface terminations, i.e.,

S1-Ce, S1-Rh2, S2-Ce, and S2-As terminations, which may result in different surface states [47].

To examine possible termination effects, we focused the beam down 15×15 μm^2 and performed a systematic position and sample dependence scan. Figure 13 summarizes the measured representative intensity plots. One can see that Figs. 13(b)–13(d) are overall very similar to each other for different spots within the same sample. The measured band spectra can be reasonably reproduced by the calculated bulk-electronic structure, suggesting their bulk nature. To further pin down their origin, we extracted the measured band dispersions and plotted them together with the corresponding soft x-ray ARPES data [Figs. 13(f)–13(h)]. It is clear that they are almost identical to each other, which directly proves the bulk nature of them. On the other hand, from the observation of large
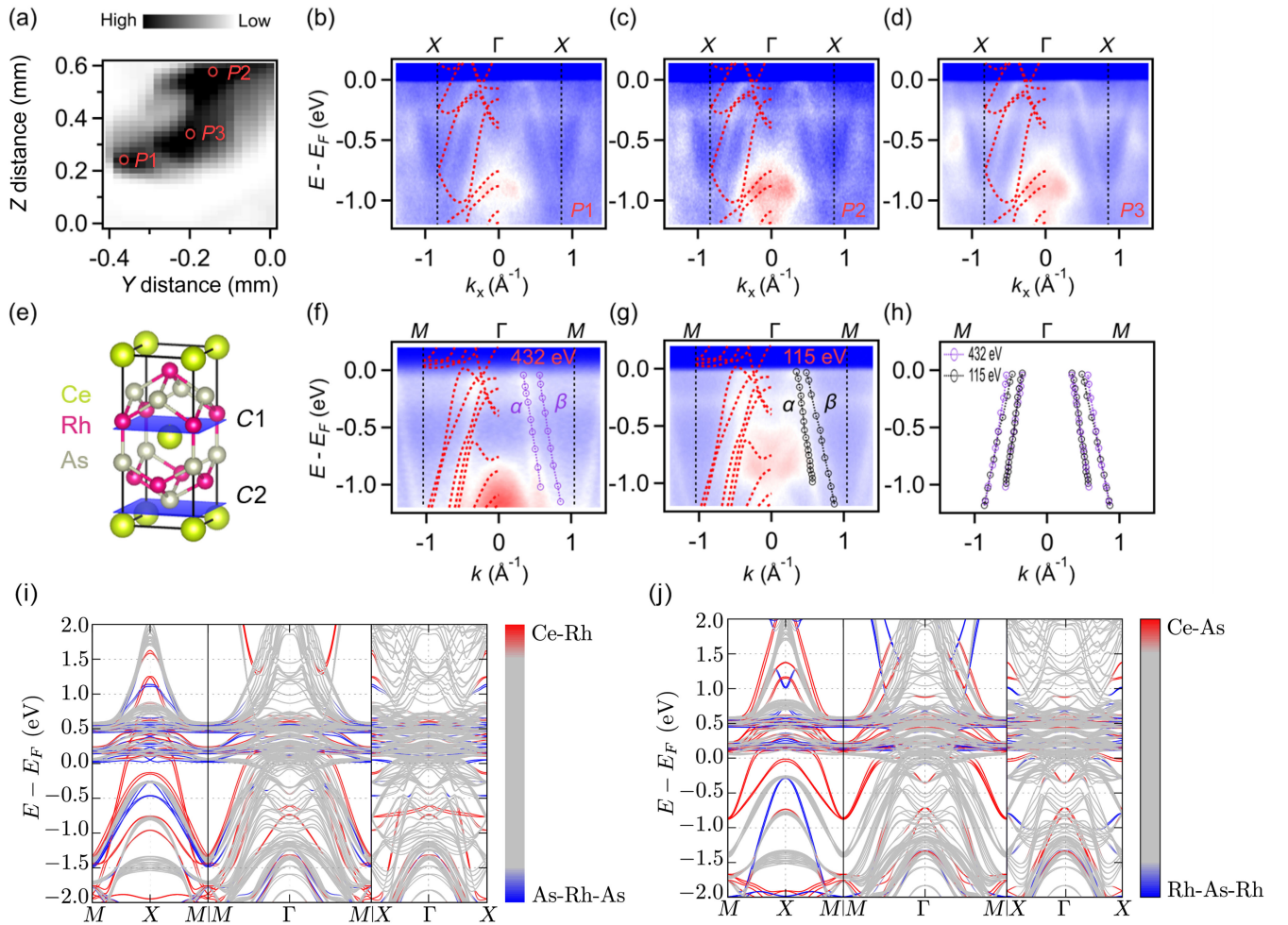

FIG. 13. (a) Photoemission intensity as a function of the displacement distance of the Y and Z axes obtained by controlling the sample manipulator to move automatically with steps of 0.02 mm. The beam spot is approximately 15×15 μm^2. (b)–(d) ARPES intensity plots of CeRh$_2$As$_2$ along the $\Gamma - X$ direction taken with 115 eV photon energy at different positions labeled by the red circle in (a). (e) Crystal structure of CeRh$_2$As$_2$. Two possible cleavage planes are shown by blue planes labeled $C1$, $C2$ respectively. (f), (g) Soft-x-ray (432 eV) and VUV (115 eV) ARPES intensity plots along the $\Gamma - M$ direction. (h) Comparison of the dispersions of the two conduction bands α, β taken with 115- and 432-eV photons. For comparison, the calculated band structures along $\Gamma - X$ and $\Gamma - M$ are superposed on the experimental data in (b)–(d) and (f),(g). (i),(j) The slablike calculation for four different surface terminations adapted from Ref. [47]. Panels (b)–(d) and (g) were taken with nonpolarized light.
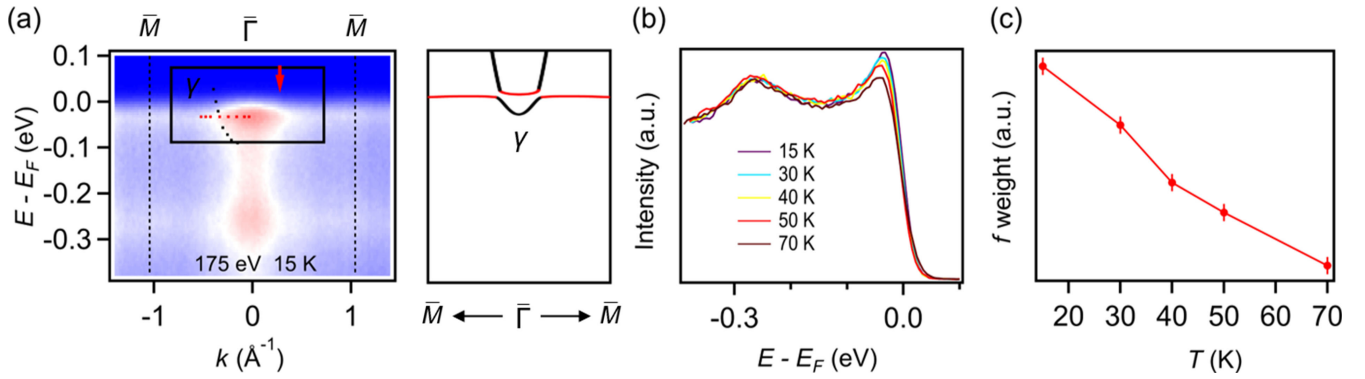
FIG. 14. Heavy $4f$-electron flat bands by temperature-dependent ARPES experiments. (a) ARPES intensity plots of $CeRh_2As_2$ along $\bar{\Gamma} - \bar{M}$ at the labeled photon energy and temperature with linear vertical (LV) polarization. Schematic illustration of the hybridization between f electrons (red) and a conduction band (black) corresponding to the black rectangle area in the left panel. (b) Temperature dependence of the EDCs indicated by red arrows in (a). (c) Temperature dependence of the quasiparticle spectral weight near E_F integrated over ($E_F - 100$ meV, $E_F + 10$ meV).

background intensity, we speculated that cleave-induced surface disorder and scatterings disrupt the surface states, as has also been observed in other materials like molybdenum phosphide [90].

APPENDIX E: TEMPERATURE-DEPENDENT ARPES MEASUREMENTS NEAR THE BULK-ELECTRON γ BAND

In the main text, we delved into the hybridization between the bulk hole α pocket and the $4f_{5/2}^1$ band. To further illustrate this, Fig. 14 presents the results of temperature-dependent ARPES experiments conducted near the bulk-electron γ pocket band. As expected, these results exhibit a temperature evolution similar to that of the α band. This consistency strengthens our assertion that the observed Kondo hybridization is predominantly contributed by bulk bands.

APPENDIX F: SCHEMATIC ILLUSTRATION OF THE ARPES EXPERIMENTAL SETUP

The experimental setup for polarization-dependent ARPES is shown in Fig. 15. For the LH (or LV)
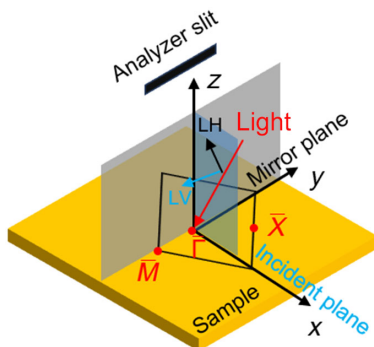

FIG. 15. Schematic illustration of the ARPES experimental setup.

experimental geometry, the electric field direction of the incident photons is parallel (or perpendicular) to the incident plane defined by the incident beam and the sample surface normal.

[1] R. Markiewicz, *A survey of the Van Hove scenario for high-T_c superconductivity with special emphasis on pseudogaps and striped phases*, J. Phys. Chem. Solids **58**, 1179 (1997).
[2] W.-S. Wang, Z.-Z. Li, Y.-Y. Xiang, and Q.-H. Wang, *Competing electronic orders on kagome lattices at Van Hove filling*, Phys. Rev. B **87**, 115135 (2013).
[3] M. L. Kiesel, C. Platt, and R. Thomale, *Unconventional Fermi surface instabilities in the kagome Hubbard model*, Phys. Rev. Lett. **110**, 126405 (2013).
[4] D. M. Newns, C. C. Tsuei, and P. C. Pattnaik, *Van Hove scenario for d-wave superconductivity in cuprates*, Phys. Rev. B **52**, 13611 (1995).
[5] V. Y. Irkhin, A. A. Katanin, and M. I. Katsnelson, *Robustness of the Van Hove scenario for high T_c superconductors*, Phys. Rev. Lett. **89**, 076401 (2002).
[6] W.-G. Yin, C.-D. Gong, and P. W. Leung, *Origin of the extended Van Hove region in cuprate superconductors*, Phys. Rev. Lett. **81**, 2534 (1998).
[7] D. M. Newns *et al.*, *Van Hove scenario for cuprate superconductivity*, Physica (Amsterdam) **186-188B**, 801 (1993).
[8] D. M. Newns, P. C. Pattnaik, and C. C. Tsuei, *Role of Van Hove singularity in high-temperature superconductors: Mean field*, Phys. Rev. B **43**, 3075 (1991).
[9] R. S. Markiewicz, B. Singh, C. Lane, and A. Bansil, *High-order Van Hove singularities in cuprates and related high-T_c superconductors*, arXiv:2105.04546.
[10] J. G. Storey, J. L. Tallon, and G. V. M. Williams, *Saddle-point van Hove singularity and the phase diagram of high-T_c cuprates*, Phys. Rev. B **76**, 174522 (2007).
[11] J. Bouvier, J. Bok, and S. Alexandrov, *Electron-phonon interaction in the high-cuprates in the framework of the Van Hove scenario*, Adv. Condens. Matter Phys. **2010**, 1 (2010).

[12] J. Bok, *Superconductivity in the cuprates. The Van Hove scenario*, Physica (Amsterdam) **209C,** 107 (1993).

[13] D. M. Newns, C. C. Tsuei, R. P. Huebener, P. J. M. van Bentum, P. C. Pattnaik, and C. C. Chi, *Quasiclassical transport at a Van Hove singularity in cuprate superconductors*, Phys. Rev. Lett. **73,** 1695 (1994).

[14] C. C. Tsuei, D. M. Newns, C. C. Chi, and P. C. Pattnaik, *Anomalous isotope effect and Van Hove singularity in superconducting Cu oxides*, Phys. Rev. Lett. **65,** 2724 (1990).

[15] P. Majumdar and H. R. Krishnamurthy, *Van Hove singularity effects in strongly correlated fermions*, arXiv:cond-mat/9604057.

[16] M. E. Barber, A. S. Gibbs, Y. Maeno, A. P. Mackenzie, and C. W. Hicks, *Resistivity in the vicinity of a Van Hove singularity:* Sr_2RuO_4 *under uniaxial pressure*, Phys. Rev. Lett. **120,** 076602 (2018).

[17] D. Fang, X. Shi, Z. Du, P. Richard, H. Yang, X. X. Wu, P. Zhang, T. Qian, X. Ding, Z. Wang *et al.*, *Observation of a Van Hove singularity and implication for strong-coupling induced Cooper pairing in* KFe_2As_2, Phys. Rev. B **92,** 144513 (2015).

[18] Y. Luo *et al.*, *A unique Van Hove singularity in kagome superconductor* $CsV_{3-x}Ta_xSb_5$ *with enhanced superconductivity*, Nat. Commun. **14,** 3819 (2023).

[19] M. Kang *et al.*, *Twofold van Hove singularity and origin of charge order in topological kagome superconductor* CsV_3Sb_5, Nat. Phys. **18,** 301 (2022).

[20] T. Park, M. Ye, and L. Balents, *Electronic instabilities of kagome metals: Saddle points and Landau theory*, Phys. Rev. B **104,** 035142 (2021).

[21] R. Nandkishore, L. S. Levitov, and A. V. Chubukov, *Chiral superconductivity from repulsive interactions in doped graphene*, Nat. Phys. **8,** 158 (2012).

[22] W. R. B. Luckin *et al.*, *Controlling charge density order in* $2H$-$TaSe_2$ *using a Van Hove singularity*, Phys. Rev. Res. **6,** 013088 (2024).

[23] N. Regnault *et al.*, *Catalogue of flat-band stoichiometric materials*, Nature (London) **603,** 824 (2022).

[24] G. R. Stewart, *Heavy-fermion systems*, Rev. Mod. Phys. **56,** 755 (1984).

[25] S. Khim *et al.*, *Field-induced transition within the superconducting state of* $CeRh_2As_2$, Science **373,** 1012 (2021).

[26] D. Hafner *et al.*, *Possible quadrupole density wave in the superconducting Kondo lattice* $CeRh_2As_2$, Phys. Rev. X **12,** 011023 (2022).

[27] M. Kibune *et al.*, *Observation of antiferromagnetic order as odd-parity multipoles inside the superconducting phase in* $CeRh_2As_2$, Phys. Rev. Lett. **128,** 057002 (2022).

[28] S. Kimura, J. Sichelschmidt, and S. Khim, *Optical study of the electronic structure of locally noncentrosymmetric* $CeRh_2As_2$, Phys. Rev. B **104,** 245116 (2021).

[29] S. Kitagawa *et al.*, *Two-dimensional XY-type magnetic properties of locally noncentrosymmetric superconductor* $CeRh_2As_2$, J. Phys. Soc. Jpn. **91,** 43702 (2022).

[30] J. F. Landaeta *et al.*, *Field-angle dependence reveals odd-parity superconductivity in* $CeRh_2As_2$, Phys. Rev. X **12,** 031001 (2022).

[31] S. Mishra, Y. Liu, E. D. Bauer, F. Ronning, and S. M. Thomas, *Anisotropic magnetotransport properties of the*

[32] heavy-fermion superconductor $CeRh_2As_2$, Phys. Rev. B **106,** L140502 (2022).

[32] S. Onishi *et al.*, *Low-temperature thermal conductivity of the two-phase superconductor* $CeRh_2As_2$, Front. Electron. Mater. **2,** 880579 (2022).

[33] D. C. Cavanagh, T. Shishidou, M. Weinert, P. M. R. Brydon, and D. F. Agterberg, *Nonsymmorphic symmetry and field-driven odd-parity pairing in* $CeRh_2As_2$, Phys. Rev. B **105,** L020505 (2022).

[34] T. Hazra and P. Coleman, *Triplet pairing mechanisms from Hund's-Kondo models: Applications to* UTe_2 *and* $CeRh_2As_2$, Phys. Rev. Lett. **130,** 136002 (2023).

[35] D. Möckli, *Unconventional singlet-triplet superconductivity*, J. Phys. Conf. Ser. **2164,** 012009 (2022).

[36] D. Möckli and A. Ramires, *Superconductivity in disordered locally noncentrosymmetric materials: An application to* $CeRh_2As_2$, Phys. Rev. B **104,** 134517 (2021).

[37] D. Möckli and A. Ramires, *Two scenarios for superconductivity in* $CeRh_2As_2$, Phys. Rev. Res. **3,** 023204 (2021).

[38] K. Nogaki, A. Daido, J. Ishizuka, and Y. Yanase, *Topological crystalline superconductivity in locally noncentrosymmetric* $CeRh_2As_2$, Phys. Rev. Res. **3,** L032071 (2021).

[39] K. Nogaki and Y. Yanase, *Even-odd parity transition in strongly correlated locally noncentrosymmetric superconductors: Application to* $CeRh_2As_2$, Phys. Rev. B **106,** L100504 (2022).

[40] A. Ptok, K. J. Kapcia, P. T. Jochym, J. Łażewski, A. M. Oleś, and P. Piekarz, *Electronic and dynamical properties of* $CeRh_2As_2$: *Role of* Rh_2As_2 *layers and expected orbital order*, Phys. Rev. B **104,** L041109 (2021).

[41] A. Skurativska, M. Sigrist, and M. H. Fischer, *Spin response and topology of a staggered-Rashba superconductor*, Phys. Rev. Res. **3,** 033133 (2021).

[42] H. Siddiquee, Z. Rehfuss, C. Broyles, and S. Ran, *Pressure dependence of superconductivity in* $CeRh_2As_2$, Phys. Rev. B **108,** L020504 (2023).

[43] K. Semeniuk *et al.*, *Decoupling multiphase superconductivity from normal state ordering in* $CeRh_2As_2$, Phys. Rev. B **107,** L220504 (2023).

[44] K. Machida, *Violation of Pauli-Clogston limit in the heavy-fermion superconductor* $CeRh_2As_2$: *Duality of itinerant and localized* $4f$ *electrons*, Phys. Rev. B **106,** 184509 (2022).

[45] A. Szabo and A. Ramires, *Superconductivity-induced improper orders*, arXiv:2309.05664.

[46] E. G. Schertenleib, M. H. Fischer, and M. Sigrist, *Unusual* $H-T$ *phase diagram of* $CeRh_2As_2$: *The role of staggered noncentrosymmetricity*, Phys. Rev. Res. **3,** 023179 (2021).

[47] K. J. Kapcia and A. Ptok, *Electronic properties and surface states of* $CeRh_2As_2$, arXiv:2311.01037.

[48] J. Ishizuka, K. Nogaki, M. Sigrist, and Y. Yanase, *Correlation-induced Fermi surface evolution and topological crystalline superconductivity in* $CeRh_2As_2$, arXiv:2311.00324.

[49] H.-T. Ma, P.-F. Tian, D.-L. Guo, Y. Liu, X. Ming, X.-J. Zheng, and H. Li, *Phase evolution of Ce-based heavy-fermion superconductors under compression: A combined first-principles and effective-model study*, Phys. Rev. B **109,** 195164 (2024).

[50] D. S. Christovam, M. Ferreira-Carvalho, A. Marino, M. Sundermann, D. Takegami, A. Melendez-Sans, K. D. Tsuei, Z. Hu, S. Rossler, M. Valvidares *et al.*, *Spectroscopic evidence of Kondo-induced quasiquartet in* $CeRh_2As_2$, Phys. Rev. Lett. **132**, 046401 (2024).

[51] T. Yoshida, M. Sigrist, and Y. Yanase, *Topological crystalline superconductivity in locally noncentrosymmetric multilayer superconductors*, Phys. Rev. Lett. **115**, 027001 (2015).

[52] T. Park, M. J. Graf, L. Boulaevskii, J. L. Sarrao, and J. D. Thompson, *Electronic duality in strongly correlated matter*, Proc. Natl. Acad. Sci. U.S.A. **105**, 6825 (2008).

[53] S. Sachdev, *Quantum criticality and the phase diagram of the cuprates*, Physica (Amsterdam) **470C**, S4 (2010).

[54] K. Momma and F. Izumi, VESTA3 *for three-dimensional visualization of crystal, volumetric and morphology data*, J. Appl. Crystallogr. **44**, 1272 (2011).

[55] D. Maruyama, M. Sigrist, and Y. Yanase, *Locally noncentrosymmetric superconductivity in multilayer systems*, J. Phys. Soc. Jpn. **81**, 034702 (2012).

[56] T. Yoshida, M. Sigrist, and Y. Yanase, *Pair-density wave states through spin-orbit coupling in multilayer superconductors*, Phys. Rev. B **86**, 134514 (2012).

[57] M. H. Fischer, F. Loder, and M. Sigrist, *Superconductivity and local noncentrosymmetricity in crystal lattices*, Phys. Rev. B **84**, 184533 (2011).

[58] R. Madar, P. Chaudouet, J. P. Senateur, S. Zemni, and D. Tranqui, *New ternary pnictides with the* $CaBe_2Ge_2$-*type structure in the systems, rare-earth-Rh-P and rare-earth-Rh-As*, J. Less-Common Met. **133**, 303 (1987).

[59] J. J. Lee *et al.*, *Interfacial mode coupling as the origin of the enhancement of* T_c *in FeSe films on* $SrTiO_3$, Nature (London) **515**, 245 (2014).

[60] S. M. Young and C. L. Kane, *Dirac semimetals in two dimensions*, Phys. Rev. Lett. **115**, 126803 (2015).

[61] Z. Wu *et al.*, *Revealing the heavy quasiparticles in the heavy-fermion superconductor* $CeCu_2Si_2$, Phys. Rev. Lett. **127**, 067002 (2021).

[62] Q. Y. Chen, D. F. Xu, X. H. Niu, J. Jiang, R. Peng, H. C. Xu, C. H. P. Wen, Z. F. Ding, K. Huang, L. Shu *et al.*, *Direct observation of how the heavy-fermion state develops in* $CeCoIn_5$, Phys. Rev. B **96**, 045107 (2017).

[63] G. Poelchen *et al.*, *Unexpected differences between surface and bulk spectroscopic and implied Kondo properties of heavy fermion* $CeRh_2Si_2$, npj Quantum Mater. **5**, 70 (2020).

[64] M. Mende *et al.*, *Strong Rashba effect and different* f–d *hybridization phenomena at the surface of the heavy-fermion superconductor* $CeIrIn_5$, Adv. Electron. Mater. **8**, 2100768 (2022).

[65] S. Patil *et al.*, *ARPES view on surface and bulk hybridization phenomena in the antiferromagnetic Kondo lattice* $CeRh_2Si_2$, Nat. Commun. **7**, 11029 (2016).

[66] G. Poelchen *et al.*, *Interlayer coupling of a two-dimensional Kondo lattice with a ferromagnetic surface in the antiferromagnet* $CeCo_2P_2$, ACS Nano **16**, 3573 (2022).

[67] D. V. Vyalikh *et al.*, k *dependence of the crystal-field splittings of* $4f$ *states in rare-earth systems*, Phys. Rev. Lett. **105**, 237601 (2010).

[68] S. Danzenbächer *et al.*, *Insight into the* f-*derived Fermi surface of the heavy-fermion compound* $YbRh_2Si_2$, Phys. Rev. Lett. **107**, 267601 (2011).

[69] M. Güttler *et al.*, *Visualizing the Kondo lattice crossover in* $YbRh_2Si_2$ *with Compton scattering*, Phys. Rev. B **103**, 115126 (2021).

[70] K. Kummer, S. Patil, A. Chikina, M. Guttler, M. Hoppner, and A. Generalov, S. Danzenbacher, S. Seiro, A. Hannaske, C. Krellner *et al.*, *Temperature-independent Fermi surface in the Kondo lattice* $YbRh_2Si_2$, Phys. Rev. X **5**, 011028 (2015).

[71] A. Damascelli, Z. Hussain, and Z.-X. Shen, *Angle-resolved photoemission studies of the cuprate superconductors*, Rev. Mod. Phys. **75**, 473 (2003).

[72] Q. Si and F. Steglich, *Heavy fermions and quantum phase transitions*, Science **329**, 1161 (2010).

[73] Y. Cao *et al.*, *Unconventional superconductivity in magic-angle graphene superlattices*, Nature (London) **556**, 43 (2018).

[74] J. F. Landaeta *et al.*, *Conventional type-II superconductivity in locally noncentrosymmetric* $LaRh_2As_2$ *single crystals*, Phys. Rev. B **106**, 014506 (2022).

[75] D. Möckli, Y. Yanase, and M. Sigrist, *Orbitally limited pair-density-wave phase of multilayer superconductors*, Phys. Rev. B **97**, 144508 (2018).

[76] T. M. Rice and G. K. Scott, *New mechanism for a charge-density-wave instability*, Phys. Rev. Lett. **35**, 120 (1975).

[77] T. Chen, H. Siddiquee, Z. Rehfuss, S. Gao, C. Lygouras, J. Drouin, V. Morano, K. Avers, C. Schmitt, A. Podlesnyak, S. Ran, Y. Song, and C. Broholm, *Quasi-two-dimensional antiferromagnetic spin fluctuation in the spin-triplet superconductor candidate* $CeRh_2As_2$, arXiv:2406.03566.

[78] N. F. Q. Yuan, H. Isobe, and L. Fu, *Magic of high-order Van Hove singularity*, Nat. Commun. **10**, 5769 (2019).

[79] R. Resta, *The insulating state of matter: A geometrical theory*, Eur. Phys. J. B **79**, 121 (2011).

[80] Päivi Törmä, Sebastiano Peotta, and Bogdan A. Bernevig, *Superconductivity, superfluidity, and quantum geometry in twisted multilayer systems*, Nat. Rev. Phys. **4**, 528 (2022).

[81] E. Rossi, *Quantum metric and correlated states in two-dimensional systems*, Curr. Opin. Solid State Mater. Sci. **25**, 100952 (2021).

[82] T. Kitamura, A. Daido, and Y. Yanase, *Spin-triplet superconductivity from quantum-geometry-induced ferromagnetic fluctuation*, Phys. Rev. Lett. **132**, 036001 (2024).

[83] T. Yoshida, M. Sigrist, and Y. Yanase, *Parity-mixed superconductivity in locally non-centrosymmetric system*, J. Phys. Soc. Jpn. **83**, 013703 (2014).

[84] S. Peotta and P. Törmä, *Superfluidity in topologically nontrivial flat bands*, Nat. Commun. **6**, 8944 (2015).

[85] J.-W. Rhim, K. Kim, and B.-J. Yang, *Quantum distance and anomalous Landau levels of flat bands*, Nature (London) **584**, 59 (2020).

[86] B. Lv, T. Qian, and H. Ding, *Angle-resolved photoemission spectroscopy and its application to topological materials*, Nat. Rev. Phys. **1**, 609 (2019).

[87] P. Blaha, K. Schwarz, G. K. H. Madsen, D. Kvasnicka, J. Luitz, R. Laskowski, F. Tran, and L. Marks, *WIEN2k, an augmented plane wave + local orbitals program for*

calculating crystal properties, Karlheinz Schwarz, Techn. Universitat Wien, Austria, 2018.

[88] M. T. Czyżyk and G. A. Sawatzky, *Local-density functional and on-site correlations: The electronic structure of* La$_2$CuO$_4$ *and* LaCuO$_3$, Phys. Rev. B **49**, 14211 (1994).

[89] Y. Wu *et al.*, *Quasi-two-dimensional Fermi surface and heavy quasiparticles in* CeRh$_2$As$_2$, arXiv:2309.06732.

[90] B. Q. Lv *et al.*, *Observation of three-component fermions in the topological semimetal molybdenum phosphide*, Nature (London) **546**, 627 (2017).